Hemodynamic impact of surgical suturing on pulmonary artery: A fluid–structure interaction analysis across varying bifurcation angles

RESEARCH ARTICLE | NOVEMBER 19 2025

Hemodynamic impact of surgical suturing on pulmonary artery: A fluid–structure interaction analysis across varying bifurcation angles

Bo Xu; Shaokoon Cheng; Ruiping Ma; Xiaodong Wang ; Yong Zhang; Zhonghua Sun ; Bernard Allard ; Jingliang Dong

Physics of Fluids 37, 111912 (2025)
https://doi.org/10.1063/5.0296213

Physics of Fluids ARTICLE pubs.aip.org/aip/pof

Hemodynamic impact of surgical suturing on pulmonary artery: A fluid–structure interaction analysis across varying bifurcation angles

Cite as: Phys. Fluids **37**, 111912 (2025); doi: 10.1063/5.0296213
Submitted: 13 August 2025 · Accepted: 28 October 2025 ·
Published Online: 19 November 2025

Bo Xu,[1,2] Shaokoon Cheng,[3] Ruiping Ma,[2,4] Xiaodong Wang,[1] Yong Zhang,[5] Zhonghua Sun,[6,7] Bernard Allard,[8] and Jingliang Dong[2,9,a)]

AFFILIATIONS

[1]School of Mechanical Engineering and Automation, Northeastern University, Shenyang 110819, People's Republic of China
[2]Institute for Sustainable Industries & Liveable Cities, Victoria University, Melbourne, Victoria 8001, Australia
[3]School of Engineering, Faculty of Science and Engineering, Macquarie University, Sydney, New South Wales 2109, Australia
[4]Department of Otolaryngology Head and Neck Surgery, The Second Affiliated Hospital of Xi'an Jiaotong University, Xi'an 710004, People's Republic of China
[5]Department of Cardiovascular Surgery, General Hospital of Northern Theater Command, Shenyang, People's Republic of China
[6]Curtin Medical School, Curtin University, Perth, Western Australia, Australia
[7]Curtin Medical Research Institute (Curtin MRI), Curtin University, Perth, Western Australia, Australia
[8]Department of Vascular Surgery, Western Health, Footscray, Victoria 3011, Australia
[9]Victoria University, Footscray Park Campus, Footscray, Victoria 3011, Australia

[a)]**Author to whom correspondence should be addressed:** jingliang.dong@vu.edu.au

ABSTRACT

Right ventricular outflow tract (RVOT) reconstruction has been widely used in the treatment of congenital heart disease. However, surgical interventions for this procedure vary due to inter-patient variations in anatomical structures of the T-shaped pulmonary bifurcation artery between patients. While postoperative hemodynamic conditions, including static pressure, arterial wall stress, and arterial vessel volume changes, play a critical role in determining long-term recovery outcomes and are largely underpinned by bifurcation angles, the impact of the latter variable on the successful outcome of RVOT remains unclear. This paper presents a numerical investigation of a realistic pulmonary artery trunk and its branches following virtual RVOT surgery by using the fluid–structure interaction modeling approach. The impact of bifurcation angles, resulting from surgical suturing, on hemodynamics and pulsatile deformation behavior of the arterial wall is systematically delineated as a function of five bifurcation angles. The results demonstrated that the bifurcation angle significantly affects local wall shear stress (WSS), static pressure distribution, and arterial volume changes throughout the cardiac cycle. Among all configurations, the model with $\alpha = 90^{\circ}$ exhibited the lowest peak WSS and the most uniform time-averaged WSS distribution, suggesting a more favorable shear environment for endothelial health. Additionally, this model showed moderate arterial volume expansion (~2.6%), indicating a balanced compliance response under pulsatile flow conditions. This study underscores the importance of considering bifurcation geometry in vascular reconstruction and highlights the value of patient-specific modeling in evaluating postoperative geometries and optimizing vascular reconstruction strategies.

NOMENCLATURE

CFD	Computational fluid dynamics
CHD	Congenital heart disease
CT	Computed tomography
FSI	Fluid–solid interaction
LPA	Left pulmonary artery
MPA	Main pulmonary artery
MRI	Magnetic resonance imaging
RPA	Right pulmonary artery
RVOT	Right ventricular outflow tract
WSS	Wall shear stress

I. INTRODUCTION

Congenital heart diseases (CHDs) represent the most common type of birth defect globally, affecting millions of newborns every year. According to the latest data released by the World Health Organization (WHO) in 2023, approximately 240 000 newborns die from congenital diseases within 28 days of birth each year.[1] The global burden of CHDs is substantial, not only in terms of prevalence but also in healthcare costs and mortality rates. The direct economic losses worldwide have been predicted to reach US$5 billion each year.[2] Despite advances in surgical techniques and postoperative care, reinterventions after right ventricle outflow tract (RVOT) reconstruction with valve substitutes remain an inevitable protocol for most patients in their lifetime,[3] highlighting the need to select and prolong the effectiveness of these surgical techniques in patients.

RVOT reconstruction is often required for the surgical management of complex pulmonary artery stenosis, particularly when associated with right ventricular outflow tract obstruction or congenital heart defects. Existing research findings in this area have irrefutably demonstrated that the change in hemodynamics before and after the surgical intervention was associated with patient's surgical outcome and their postoperative recovery.[4,5]

Corno and Mickaily-Huber[6] demonstrated the potential working principles of the catheter suture method, including the conventional "circular" and oblique "elliptical" configuration of the distal anastomosis. Their results demonstrated that clinical application of "elliptical" anastomosis, with a cross-sectional area larger than conventional "circular" anastomosis, may reduce the incidence and the degree of distal stenosis, particularly for small-size conduits. Subsequently, the scheme of using homologous or heterologous conduits to reshape the right ventricular outflow tract was proposed in the clinic.[7,8] For the structural design of vascular replacement conduits, the angle between the pulmonary trunk and the pulmonary artery will significantly affect the distribution of mechanical stress.[9–11] Under different pulmonary artery flow rates, the energy loss in the surgical area differs by two times.[12,13] Excluding postoperative complications, whether various conduits can meet their performance requirements in terms of blood fluid mechanics after surgery is an urgent issue to be verified.[14–17]

Advancements in computational fluid dynamics (CFD), coupled with its increasing acceptance in surgical planning, have led to its widespread adoption for evaluating and predicting surgical outcomes over the past decade. This approach allows for a clearer visualization of different surgical plans and the prediction of postoperative outcomes. In particular, CFD provides detailed insights by resolving highly complex flow fields at different regions of the flow domain, which is valuable information that traditional imaging techniques cannot provide.[18–21] To briefly contextualize the current research landscape, several representative studies adopting CFD in pulmonary circulation modeling are reviewed.

Yang *et al.* developed a numerical method to simulate fluid–structure interaction (FSI) in a 3D idealized model of a pulmonary arterial bifurcation with collapsible tubes. Their findings revealed that both upstream and downstream regions of the collapsed tube exhibited recirculation zones and increased flow resistance.[22] Bordones *et al.* investigated hemodynamic flow patterns in the pulmonary artery using particle image velocimetry (PIV) and CFD modeling. In their study, a patient-specific pulmonary artery geometry was used to manufacture a transparent phantom via rapid prototyping. Velocity fields and shear stress distributions were extracted for direct comparison between CFD and PIV data. Their results confirmed the accuracy of CFD for predicting pulmonary circulation hemodynamics.[23] Ebrahimi *et al.* advanced pulmonary hemodynamics modeling by presenting a multi-scale approach that integrates 3D flow dynamics in major vessels with an anatomically based vascular network. This model accounts for multiple factors influencing capillary perfusion and enabled estimation of postural effects on wall shear stress (WSS) in the bilaterial pulmonary arteries.[23] More recently, Tsubata *et al.* used CFD to evaluate pulmonary artery blood flow in patients with chronic thromboembolic pulmonary hypertension (CTEPH) before and after pulmonary endarterectomy and balloon pulmonary angioplasty. Their patient-specific analysis showed that the pulmonary endarterectomy induced redistribution of pulmonary blood flow and improved blood flow dynamics in the pulmonary artery.[24]

Despite numerous studies on pulmonary artery blood flow, previous efforts have primarily focused on revealing haemodynamic flow patterns in either simplified or patient-specific pulmonary artery models. However, inter-subject variation—particularly in relation to virtual surgical plans—has not been thoroughly investigated. Numerical simulations offer unique insights into blood flow dynamics and wall compliance behavior that remain inaccessible through traditional imaging techniques. Therefore, exploring the haemodynamic factors influencing surgical outcomes is essential to assist vascular surgeons to better understand these variations and support the development of optimal surgical strategies.[25]

To address this research gap, this study developed a series of pulmonary artery bifurcation models that simulated virtual operations of RVOT reconstruction, with varying vascular branch angles representing potential surgical suturing outcomes. By incorporating a fluid–structure interaction modeling approach, the effects of arterial wall compliance were investigated across all models. Key haemodynamic parameters, including wall shear stress, wall pressure, and arterial volume change, were extracted for comparative analysis. The proposed numerical modeling framework and findings are expected to aid in the optimization of the RVOT surgical planning and offer insights into the management of postoperative vascular collapse resulting from structural changes during vascular remodeling.

II. MATERIALS AND METHODS

A. Geometry reconstruction of artery models

Prior to commencing this study, ethical approval was obtained from the Medical Ethics Committee of Cardiovascular Surgery and the Institutional Review Board of the General Hospital of Northern Theater Command, Shenyang, China (Batch No.: 2020-15). Written informed consent was obtained from the guardians of all pediatric participants involved in this research.

In this study, magnetic resonance imaging (MRI) was performed on an 11-year-old child with congenital heart dysplasia and pulmonary artery stenosis (Fig. 1). The imaging data were acquired with a resolution of 0.405×0.405 mm, with a slice increment of 0.5 mm. Patient-specific arterial geometry was extracted using the open-access software 3D Slicer (Version 5.6.2, https://www.slicer.org). The three-dimensional geometry was saved in standard tessellation language (STL) format.

Although the original patient-specific model was reconstructed from MRI data of a diseased pulmonary artery with stenosis, the

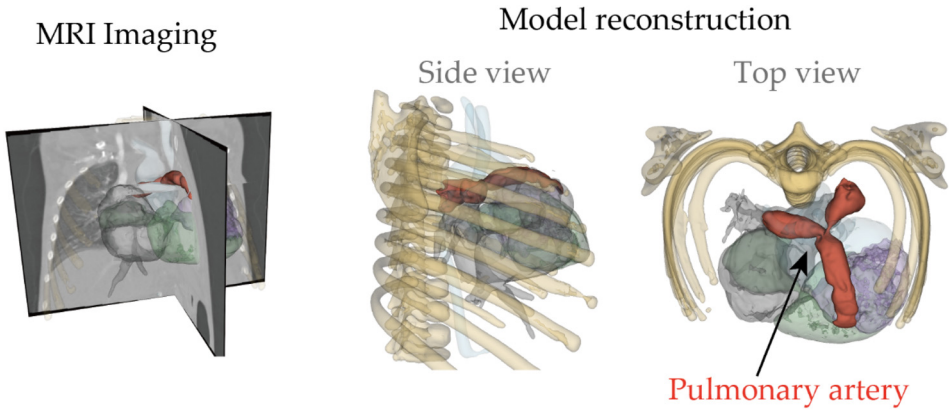

FIG. 1. Patient-specific pulmonary artery reconstructed from MRI images.

objective of this study was not to assess pathological hemodynamics *per se*, but rather to investigate the post-surgical hemodynamic consequences of varying bifurcation angles between the main pulmonary artery (MPA) and the right pulmonary artery (RPA). To isolate the influence of bifurcation geometry and minimize confounding anatomical irregularities, a virtual arterial repair was performed on the baseline model to remove its stenotic features and restore vessel continuity.

In this study, the bifurcation angle between the MPA and the RPA was systematically varied while maintaining a fixed angle between the RPA and LPA (the left pulmonary artery). This modeling choice reflects the surgical reality that, during patch reconstruction or anatomical repair, the positions of the branch pulmonary arteries are typically preserved, while the orientation of the reconstructed MPA can vary depending on surgical technique and tissue flexibility. This approach allows for targeted investigation of how MPA inflow direction influences bifurcation hemodynamics.

The angle between the main pulmonary artery (MPA) and the right pulmonary artery (RPA) was defined as α in this work. For the original anatomy, the α angle was 100°, closely matching the MRI imaging. To investigate the impact of different vascular suturing outcomes, the α angle was systematically varied from the original configuration. Modified virtual models were created with α angles of 70°, 80°, 90°, and 105°, in addition to the baseline model with $\alpha = 100°$. Therefore, five pulmonary artery bifurcation models were considered in this study (Fig. 2).

This approach enabled a controlled parametric investigation of bifurcation angle effects under post-operative conditions, which would not be feasible with a single, anatomically fixed diseased model. The focus of the study is therefore not comparative pathology but biomechanical optimization of surgical geometry, and the virtual repair serves as a clinically plausible baseline for evaluating surgical outcomes.

B. Computational meshing

All five pulmonary artery bifurcation models were imported into ANSYS ICEM and ANSYS Fluent (ANSYS Inc., PA, USA) to generate tetrahedral meshes for the fluid domains (blood flow). A constant arterial wall thickness of 0.43 mm[26] was assigned to the exterior of the fluid domains to represent the arterial wall (solid domain), which was meshed using the transient structural module in ANSYS mechanical.

A mesh independence test was conducted prior to the numerical simulations to determine the optimal mesh element size that balances simulation accuracy with computational efficiency. As shown in Fig. 3, three mesh densities were evaluated in this study: a coarse mesh with a characteristic element size of 2 mm (52 901 total elements); a medium mesh with a characteristic element size of 1 mm (260 010 total elements); and a fine mesh with a characteristic element size of 0.5 mm (1 466 270 total elements). All meshes were generated using a tetrahedral mesh.

To ensure accurate resolution of near-wall velocity gradients and reliable wall shear stress (WSS) prediction, a boundary layer mesh consisting of seven prism layers with an initial thickness of 0.3 mm was incorporated along the arterial walls.

Velocity data were extracted at a cross section near the bifurcation for analysis over a full cardiac cycle (Fig. 4). These results showed that the medium and fine meshes produced closely aligned velocity profiles throughout a cardiac cycle, indicating that the additional mesh refinement had minimal impact on accuracy. In contrast, the coarse mesh consistently underpredicted velocity magnitudes at the extraction plane across the entire cycle. To balance simulation accuracy and computational efficiency, the medium mesh was selected for generating the computational meshes for all five pulmonary artery models.

C. Governing equations

1. Blood flow (fluid domain)

The blood flow within the pulmonary artery was modeled as an incompressible, laminar, non-Newtonian fluid. The governing equations are based on the unsteady Navier–Stokes and continuity equations:

Continuity equation

$$\nabla \cdot \boldsymbol{u} = 0. \tag{1}$$

Momentum equation

$$\rho\left[\frac{\partial \boldsymbol{u}}{\partial t} + (\boldsymbol{u}\cdot\nabla)\boldsymbol{u}\right] = -\nabla p + \mu\nabla^2\boldsymbol{u} + \mathbf{f}, \tag{2}$$

where $\boldsymbol{u}$ is the velocity vector and p is the pressure field, which is not prescribed at the velocity inlet but instead computed as part of the solution of the Navier–Stokes equations; ρ is the fluid density

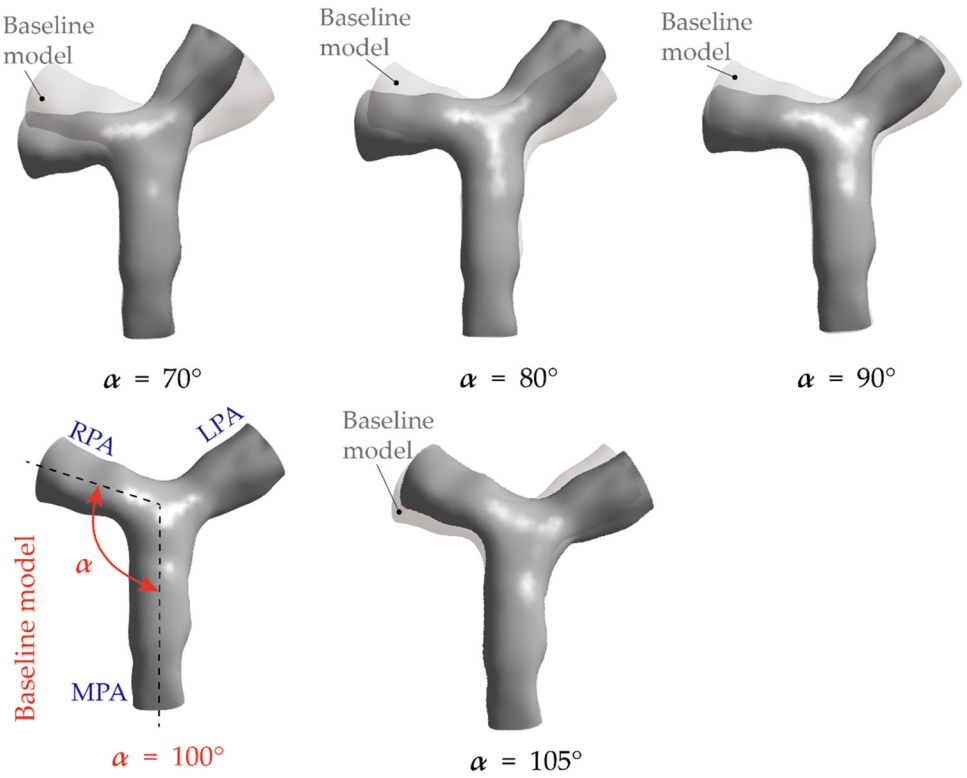

FIG. 2. Modified virtual pulmonary artery models with five different branch angles: $\alpha = 70°$, 80°, 90°, 100° (baseline), and 105°.

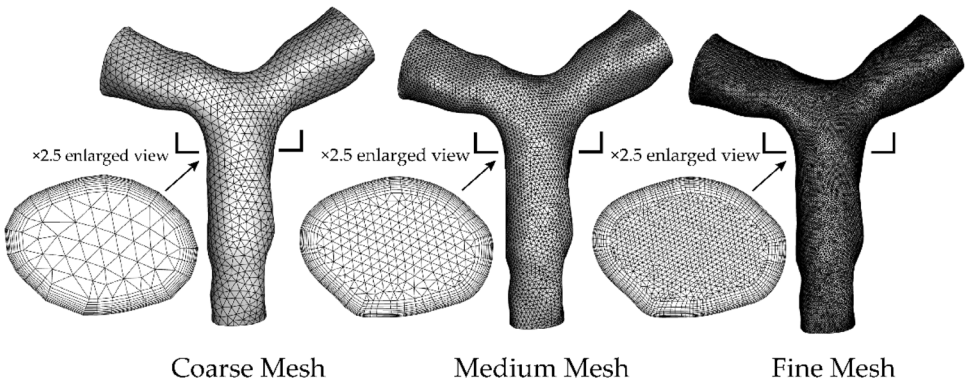

FIG. 3. Surface mesh preview of the baseline model ($\alpha = 100°$) by adopting three levels of mesh density: the coarse mesh, the medium mesh, and the fine mesh.

1060 kg/m^3; μ is the dynamic viscosity of blood; $\boldsymbol{f}$ represents body forces, specifically gravity acting along the negative z-axis.

In this study, the blood viscosity μ was modeled as a non-Newtonian fluid using the Carreau model, with the following constants: $\mu_0 = 0.056$ Pa s, $\mu_\infty = 0.0035$ Pa s, $\lambda = 3.3568$ s, and $n = 0.3568$.

All governing equations were solved using the finite volume method (FVM) within ANSYS Fluent. A no-slip condition was applied to all arterial wall boundaries in the pulmonary artery models.

2. Arterial wall (structural domain)

The arterial wall was modeled as a deformable structure using the principles of isotropic elasticity with Young's modulus of 0.9 MPa and Poisson's ratio of 0.3.[14,27] The governing equation for structural dynamics is

$$\rho_s \frac{\partial^2 \boldsymbol{d}}{\partial t^2} = \nabla \cdot \sigma + \boldsymbol{f}_s, \tag{3}$$

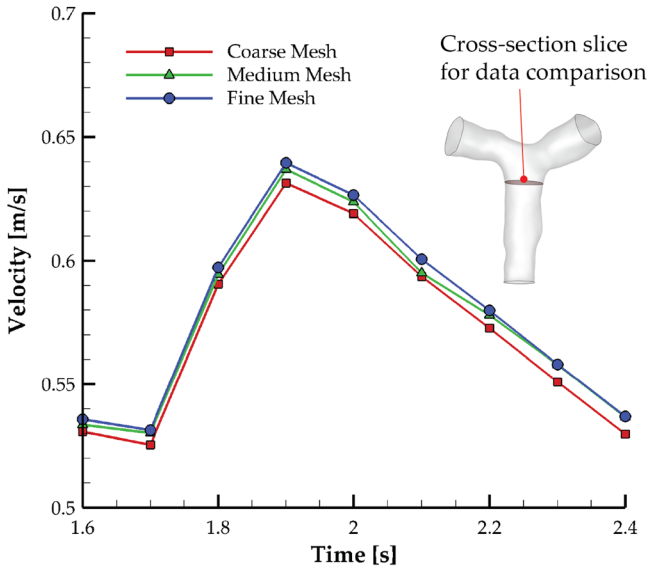

FIG. 4. Mesh independence test: transient velocity profiles were extracted at a cross section upstream of the pulmonary bifurcation of the baseline model. Only velocity data from the 3rd cardiac cycle were used for analysis.

where $\boldsymbol{d}$ is the displacement vector, ρ_s is the solid density (1060 kg/m^3), σ is the Cauchy stress tensor, and $\boldsymbol{f}_s$ represents body forces acting on the structure, which were assumed negligible in this study due to the relatively small mass of the pulmonary artery trunk (approximately 1.2 g).

All structural domain governing equations were solved in ANSYS transient structural using the finite element method (FEM).

3. Fluid-structure interaction (FSI) coupling

The coupling between the fluid and solid domains was performed using a two-way FSI approach within ANSYS workbench. The interface between the fluid and the structure satisfies the following conditions:

(a) Kinematic continuity (displacement matching)

$$\boldsymbol{d}_f = \boldsymbol{d}_s \text{ on the interface.} \tag{4}$$

(b) Dynamic continuity (traction equilibrium)

$$\boldsymbol{\sigma}_f \cdot \boldsymbol{n} = \boldsymbol{\sigma}_s \cdot \boldsymbol{n} \text{ on the interface,} \tag{5}$$

where $\boldsymbol{n}$ is the normal vector on the fluid–solid interface.

The kinematic continuity [Eq. (4)] ensures that the displacement of the fluid matches that of the solid, maintaining a continuous and gap-free interface. The dynamic continuity [Eq. (5)] enforces traction equilibrium, such that the stress exerted by the fluid on the structure is balanced by an equal and opposite stress from the structure. Together, these conditions ensure that the fluid and structure interact consistently, capturing the coupled motion and forces in the FSI system.

D. Boundary conditions

In this study, since the research focuses on hemodynamics in surgically repaired vessels, we adopted a representative blood flow profile

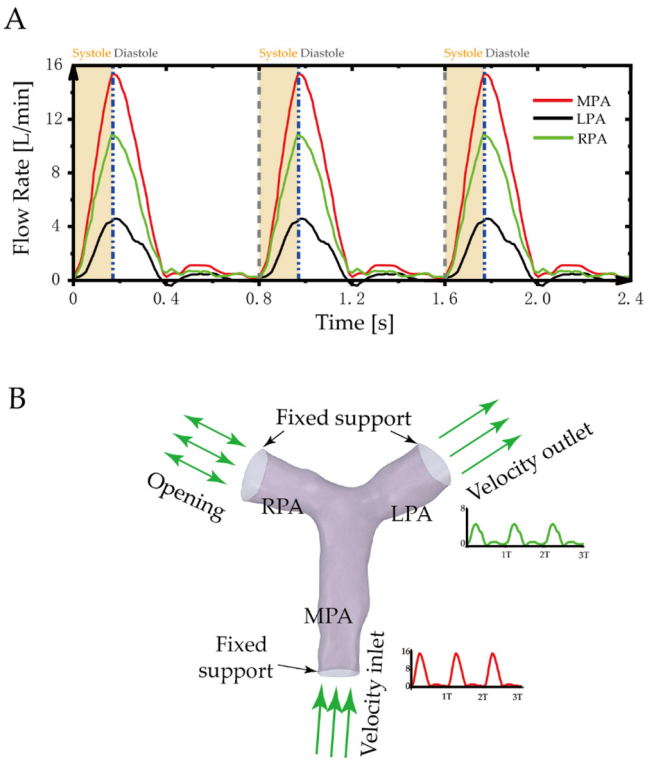

FIG. 5. (a) Blood flow profiles in the proximal pulmonary arteries under resting conditions and (b) boundary condition setup for the baseline model ($\alpha = 100°$).

from a group of healthy children (six males and four females), aged 10–14 years, as shown in Fig. 5(a). The flow data were obtained using cardiac-gated cine phase-contrast MRI (cine PC-MRI), as described by Cheng *et al.*[28]

As shown in Fig. 5(b), for the boundary conditions, the inlet of the main pulmonary artery (MPA) was defined as a velocity inlet, while the outlet of the left pulmonary artery (LPA) was set as a velocity outlet. The velocity profiles at both the inlet and outlet were calculated by dividing the volumetric flow rate by the cross-sectional area of the respective openings. The right pulmonary artery (RPA) opening was defined as an opening boundary condition, allowing flow distribution between the LPA and RPA based on the principle of mass conservation. To prevent rigid body motion during deformation, the edges at the inlets and outlets were constrained using fixed supports.

Although the peak Reynolds number during systole reaches approximately 8200, which is nominally within the turbulent regime, laminar flow was assumed for all simulations. This simplification is justified for several reasons. First, peak systole represents only a brief portion of the cardiac cycle, while the remainder occurs at significantly lower flow rates, resulting in Reynolds numbers typically within the laminar or transitional range. Second, previous studies have shown that in pulsatile arterial flows, particularly in large vessels such as the pulmonary arteries, the transient nature of peak flow combined with the shear-thinning behavior of blood, as captured by the Carreau model, can significantly suppress the onset and development of turbulence.[29] Moreover, the primary objective of this study is to assess

the influence of bifurcation angle variations in virtually repaired pulmonary arteries rather than to capture detailed turbulence dynamics. The laminar assumption, therefore enables efficient computation while preserving the reliability of comparative flow analysis.

System coupling was employed to facilitate data exchange between the fluid and structural solvers. The coupling time step was set to 0.01 s.[19] At each time step, pressure and shear stresses computed by Fluent were transferred to the structural solver as loads, and the resulting deformation of the arterial wall was sent back to the fluid solver as updated boundary motion. The mesh in the fluid domain was updated accordingly using dynamic mesh algorithms.

III. RESULTS

A. Model validation

To validate the accuracy of the numerical simulation, a reference artery model from literature based on a Y-shaped model representing the average human carotid bifurcation was adopted.[30] Using this averaged model, Buchmann *et al.*[31] conducted particle image velocimetry (PIV) measurements to obtain velocity profiles at multiple cross sections along the carotid bifurcation. Although this model does not represent a pulmonary artery, both the carotid and pulmonary arteries are proximal to the heart and are subjected to high-momentum blood flow from the main branch. Therefore, this model still offers significant value for validation purposes in the present study.

The averaged carotid bifurcation geometry and the corresponding PIV data were generously provided by Dr. Buchmann, as documented in his PhD thesis.[32] For this validation section only, numerical simulations were carried out using a mean systolic flow condition (Re = 290) and the same mesh settings as those used in the present study. A comparison between the numerical results and the PIV measurements is presented based on data extracted along selected lines (Fig. 6) and cross-sectional planes (Fig. 7).

The comparison of results, including one-dimensional line data and planar velocity vectors, shows good agreement between the PIV measurements and the CFD simulations based on a rigid-wall model. Some discrepancies are observed, particularly near the inner

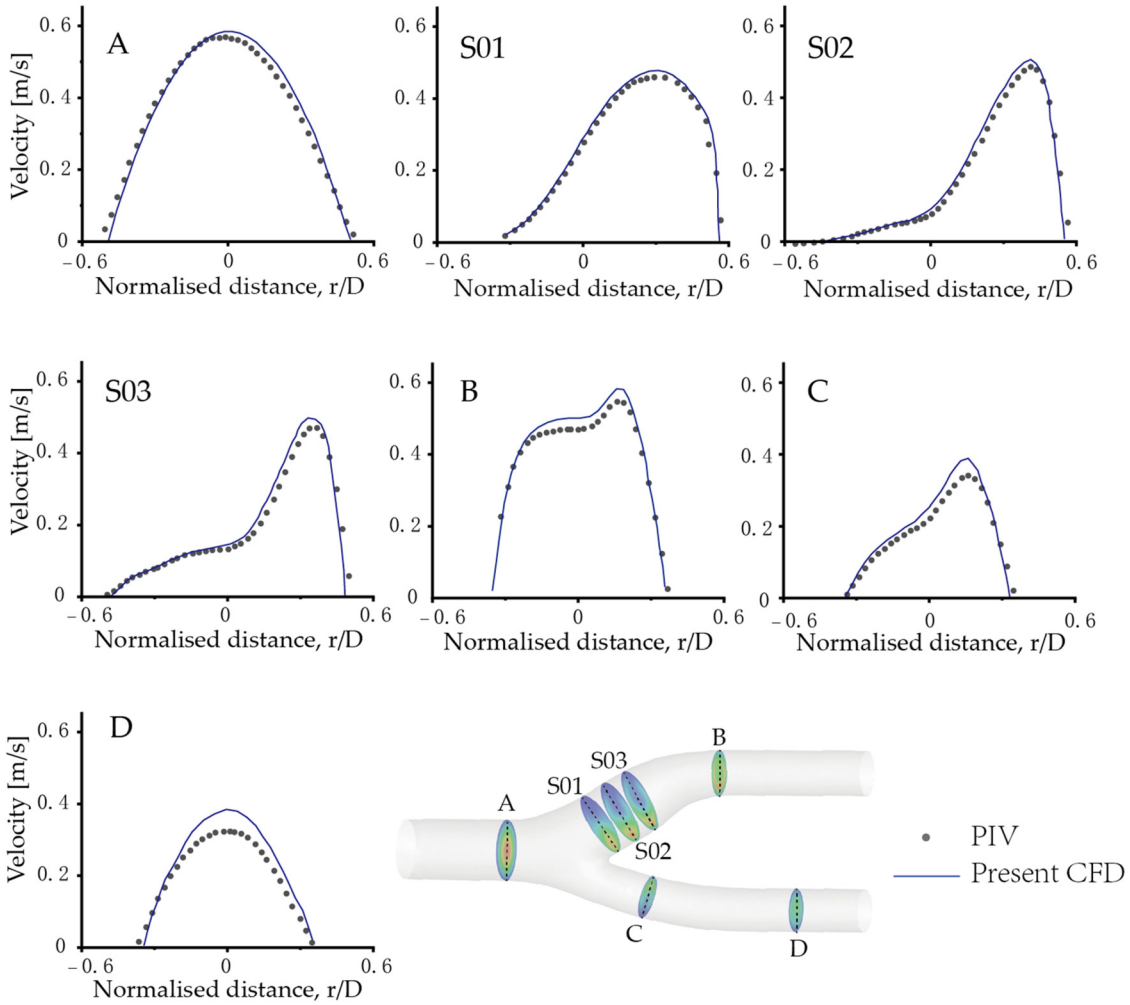

FIG. 6. Comparison of velocity profiles at selected locations between PIV measurements and the present CFD simulation using the rigid-wall model.

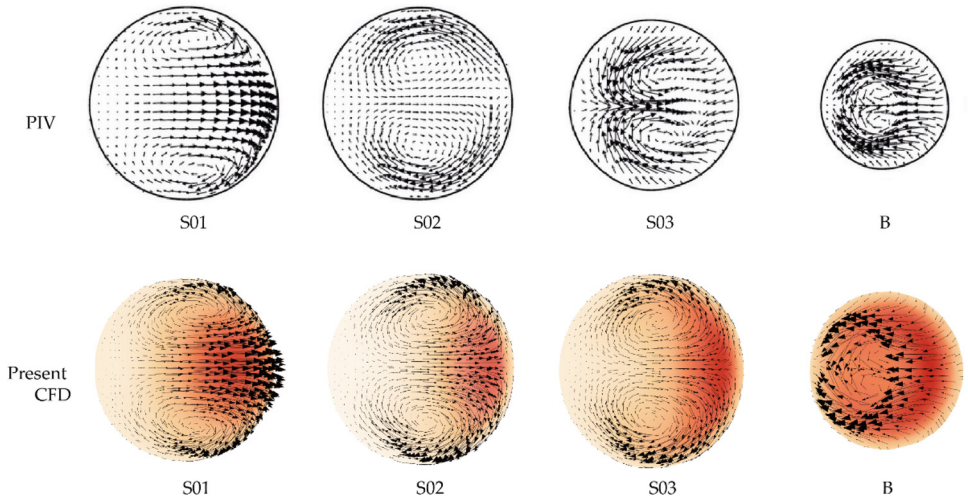

FIG. 7. Comparison of velocity vectors at selected cross-sectional planes, as shown in Fig. 6, between PIV measurements and the present CFD simulation using the rigid-wall model.

wall of the daughter branches, where skewed velocity patterns suggest uneven flow distribution. These differences may be attributed to geometric mismatches between the experimental replicas and the digital model, as the replicas are slightly larger than the original geometry. Since it is currently not feasible to perform PIV measurements on models incorporating wall compliance, the validation in this study is based on simulations using a rigid-wall assumption. Nevertheless, the observed agreement supports the reliability of the numerical approach. Although the primary focus of the present study is on FSI modeling, this validation demonstrates that the underlying computational framework is capable of accurately capturing key flow characteristics.

B. Comparison between rigid-wall and FSI models

Figure 8 compares the numerical simulation results of the baseline case ($\alpha = 100°$) between the rigid wall and FSI configurations, representing scenarios with and without wall compliance. In Fig. 8(a), the time-averaged velocity distribution shows that the FSI model achieves improved flow accommodation, with blood flow more evenly distributed across the MPA trunk. In contrast, the rigid wall model forces the flow to follow the fixed lumen geometry, resulting in more confined, directed patterns and localized high-velocity regions. This effect is particularly evident at the bifurcation into the right and the left pulmonary arteries (RPA and LPA), where the rigid anatomy constrains the flow path, leading to more abrupt flow division. In the FSI model, the compliant arterial walls deform under hemodynamic loading, allowing for dynamic adaptation of the lumen geometry, which softens the dividing flow patterns and promotes smoother redistribution.

Notably, at the MPA entrance, the FSI model exhibits a slightly higher peak velocity (2.13 m/s) compared to the rigid model (1.81 m/s). This difference is primarily attributed to arterial bending in the curved segment of the MPA, where wall deformation in the FSI simulation results in a transiently narrowed lumen that accelerates flow through that region.

Figure 8(b) shows the corresponding time-averaged wall shear stress (WSS) distributions. The FSI model demonstrates a slightly broader spatial distribution of regions with WSS exceeding 2.5 Pa. Moreover, the peak WSS values are reduced in the FSI model. This reduction is attributed to the arterial wall's ability to deform under pulsatile loading, which increases the effective fluid domain and dampens shear gradients. These findings highlight the influence of wall compliance in modulating both velocity and shear stress patterns, supporting the use of FSI models for capturing more physiologically accurate hemodynamic behavior.

It should be noted that, in the FSI model, the inlet was constrained to prevent rigid-body motion of the arterial model. While this constraint introduced localized differences to the flow development immediately downstream between the rigid and FSI solutions, these effects are confined to the proximal region close to the inlet. Additionally, as all simulations were conducted under the same boundary assumption, any such influence is systematic and therefore does not compromise the comparative analysis between branch angle configurations. Although extending the upstream geometry could further reduce such boundary effects, this would require adding synthetic anatomy beyond the imaged domain and was therefore reserved for future work.

Figure 9 compares static wall pressure contours and nodal pressure values at the bifurcation apex in the baseline model. In Fig. 9(a), the temporal pressure contour results show that the FSI modeling approach produces a broader region of elevated pressure (exceeding 1800 Pa, approximately 13.5 mm Hg). Additionally, the MPA trunk is visibly displaced outward due to wall deformation along the natural vascular curvature. In contrast, the rigid wall model exhibits localized pressure concentration at the bifurcation apex, the flow division point, which results in unrealistic wall pressure predictions because it does not account for dynamic wall motion.

Figure 9(b) presents the static pressure magnitude at the bifurcation apex over time. The rigid wall model shows a significantly higher peak pressure, reaching approximately 4500 Pa (33.75 mm Hg)

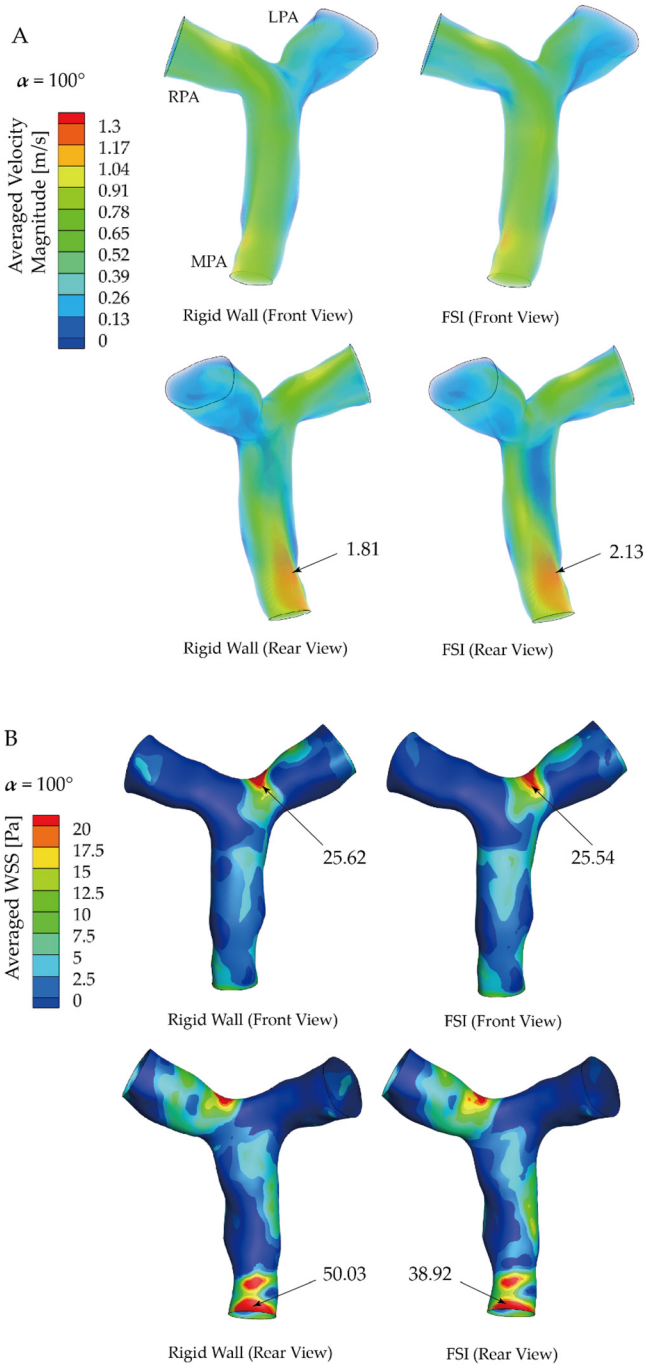

FIG. 8. Comparison of time-averaged velocity fields (a) and wall shear stress distributions (b) in the baseline artery model, using both the rigid-wall and fluid–structure interaction (FSI) methods.

at systolic peak. In comparison, the FSI model demonstrates a pressure approximately 1000 Pa lower at the same time point, reflecting the pressure-dampening effect of wall compliance, which helps absorb the pulsatile impact of blood flow.

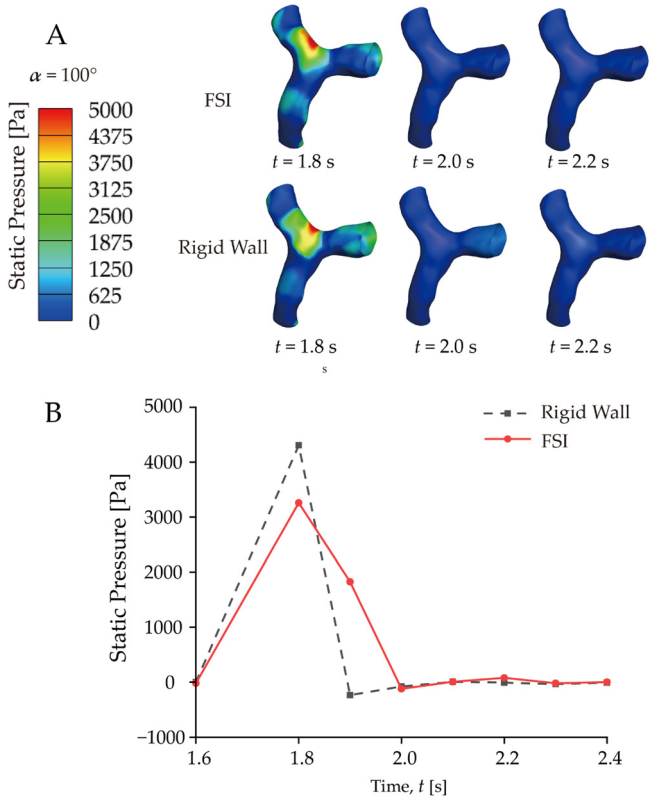

FIG. 9. Comparison of static wall pressure in the baseline artery model between rigid-wall and FSI modeling methods. (a) Static wall pressure contours at selected time points. (b) Static pressure profiles at the bifurcation apex, where pressure concentration occurs.

C. Comparison between different bifurcation angles

Figure 10 presents the FSI simulation results for all five pulmonary artery models, focusing on peak systole to evaluate the effect of bifurcation angle on arterial wall pressure distribution. The results demonstrate that the relative orientation of the MPA to the RPA and LPA significantly influences pressure patterns in the distal branches.

In the $\alpha = 70°$ model, pulsatile blood flow is more aligned with the LPA, resulting in a concentrated region of elevated wall pressure within the LPA branch. This indicates that the LPA receives the direct momentum of blood flow from the MPA with minimal damping. As the angle α gradually increases, the region of concentrated wall pressure shifts from the LPA branch toward the bifurcation apex, reaching a broadly distributed pattern at $\alpha = 90°$. At this angle, the peak pressure values are notably reduced by approximately 1700 Pa compared to all other models.

For $\alpha = 100°$ and 105°, a pronounced pressure increase is observed primarily in the proximal top side of the RPA branch, accompanied by a secondary pressure build-up along the middle outer wall of the MPA branch.

In addition to static wall pressure, Fig. 11 shows the wall shear stress (WSS) distribution at peak systole under FSI simulation conditions. Overall, all models exhibit a consistent pattern in which the RPA

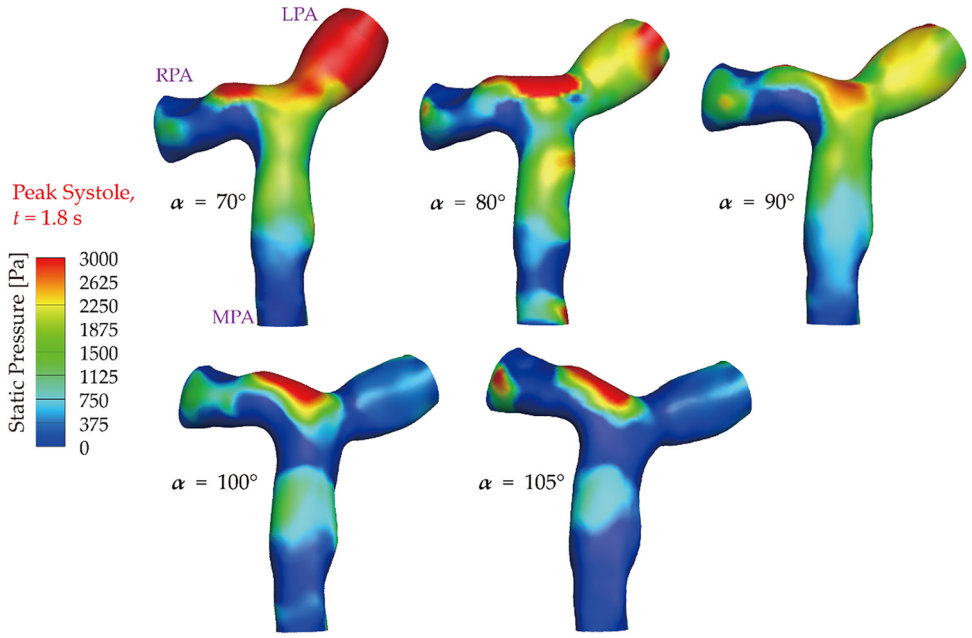

FIG. 10. Comparison of static wall pressure contours across pulmonary artery models with five different branch angles: $\alpha = 70°$, 80°, 90°, 100° (baseline), and 105° using FSI modeling.

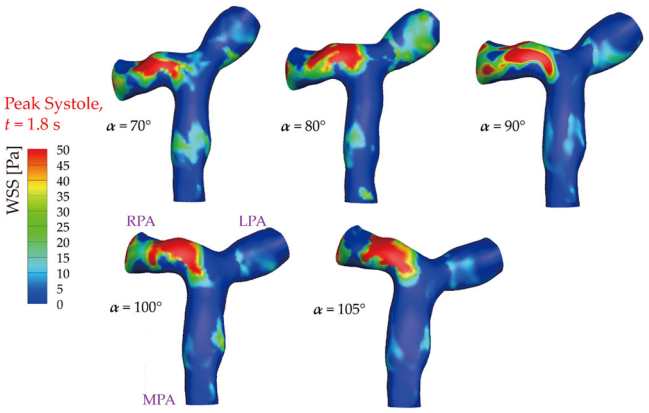

FIG. 11. Comparison of WSS contours across pulmonary artery models with five different branch angles: $\alpha = 70°$, 80°, 90°, 100° (baseline), and 105° using FSI modeling.

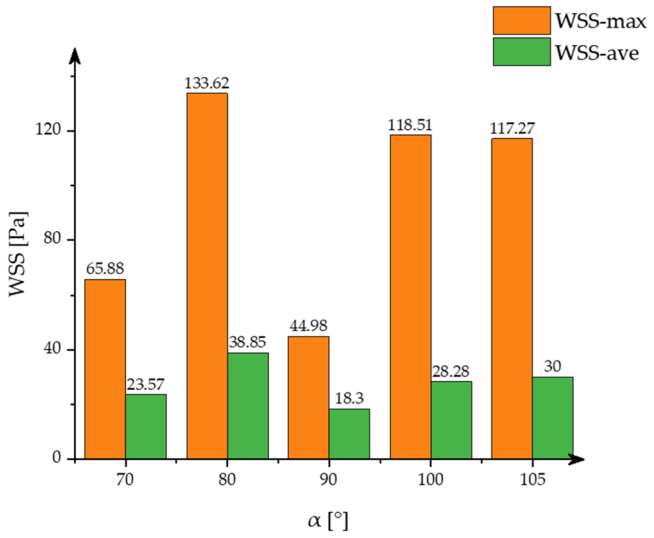

FIG. 12. Time-averaged WSS and the peak WSS values for pulmonary artery models with five different branch angles: $\alpha = 70°$, 80°, 90°, 100° (baseline), and 105° using FSI modeling.

experiences higher WSS compared to other regions of the pulmonary artery bifurcation. This is primarily due to the greater volumetric flow directed through the right branch relative to the left, resulting in increased shear forces along the RPA wall.

To quantify the WSS distribution and compare variations across the five bifurcation angle models, Fig. 12 presents both the time-averaged WSS and the peak WSS values for each case. The highest peak WSS was observed in the $\alpha = 80°$ model, reaching 133.62 Pa, followed by the $\alpha = 100°$ and $\alpha = 105°$ models, both with peak values around 118 Pa. In contrast, the $\alpha = 90°$ model exhibited the lowest peak WSS at 45 Pa.

The time-averaged WSS showed a narrower range of variation. The highest average value occurred in the $\alpha = 80°$ model at 38.85 Pa, while the lowest was again found in the $\alpha = 90°$ model, at 18.3 Pa.

These findings indicate that the $\alpha = 90°$ model exhibits both the lowest peak wall shear stress and the lowest time-averaged WSS, suggesting a more favorable hemodynamic environment for endothelial cells (ECs) compared to the other angulation configurations. Wall

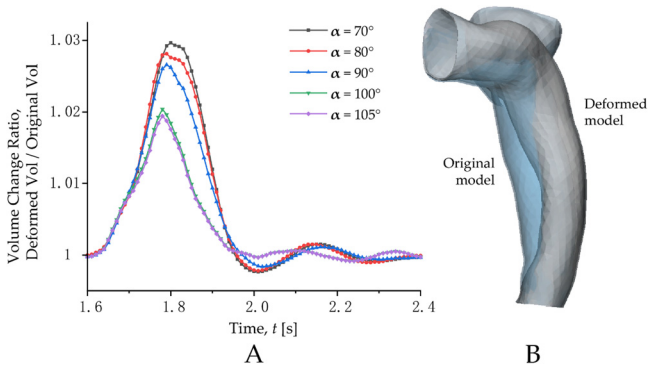

FIG. 13. Total volume change ratio profiles for pulmonary artery models with five different branch angles: $\alpha = 70°$, 80°, 90°, 100° (baseline), and 105° using FSI modeling.

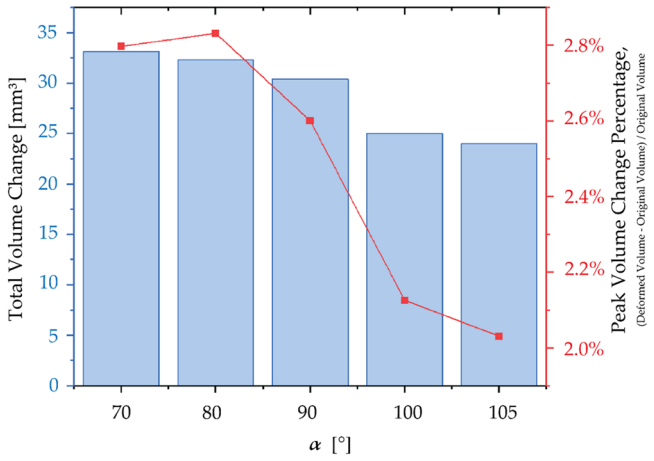

FIG. 14. Peak arterial volume change and corresponding percentage variation relative to the original vessel geometry for pulmonary artery models with five different branch angles: $\alpha = 70°$, 80°, 90°, 100° (baseline), and 105°.

shear stress is known to play a critical role in endovascular remodeling, with lower and more stable WSS levels generally associated with a reduced risk of adverse vascular changes by promoting the transformation of ECs into an anti-inflammatory phenotype and enhancing endothelial function.[33] Therefore, the $\alpha = 90°$ configuration may offer improved long-term outcomes by minimizing shear-induced remodeling following surgical intervention.

D. Arterial volume changes and clinical implications

The arterial volume change serves as a key indicator of vascular compliance and overall arterial health. Figure 13 presents the total volume change ratio profiles for all five models over a complete cardiac cycle. The volume change ratio was calculated as the ratio of the deformed (enlarged) arterial lumen volume to the original undeformed volume.

The results show that the largest vessel deformation occurs at the end of systole and the onset of diastole, reflecting the peak of pulsatile flow into the bifurcation region. Based on the deformation patterns, the five models can be grouped into two categories. Models with MPA–RPA angles (α) between 70° and 90° exhibit similar volume change ratios, peaking around 1.03. In contrast, models with angles between 100° and 105° show nearly identical profiles with lower peak values around 1.02. During the systolic phase (2.0–2.4 s), arterial deformation gradually decreases, with minor fluctuations, and the vessel returns toward its original shape.

Figure 14 summarizes the peak arterial volume change magnitudes and the corresponding variation percentages, calculated as (deformed volume–original lumen volume)/original lumen volume. The results follow the same trend observed in Fig. 13. For the $\alpha = 70°$, 80°, and 90° models, the peak volume enlargement ranges from 30 to 33 mm^3, with the $\alpha = 70°$ model showing the greatest expansion. In contrast, the $\alpha = 100°$ and 105° models exhibit lower peak volume changes, around 25 mm^3.

More pronounced differences are evident in the volume change percentages. The $\alpha = 100°$ and 105° models show an enlargement of approximately 2.0%–2.1%, while the $\alpha = 70°$, 80°, and 90° models display higher percentages, ranging from 2.6% to 2.8% relative to their original lumen volumes.

Although the absolute volume changes may appear small, even a 2% variation in arterial volume can be physiologically significant due to the confined geometry and compliance-sensitive behavior of pulmonary arteries. In vascular biomechanics, such subtle deformations can meaningfully alter local wall stress distributions, influence endothelial cell responses, and affect blood flow dynamics. Therefore, these volume changes, while modest in magnitude, reflect notable differences in vessel compliance and may have important implications for postoperative function and long-term vascular remodeling.

Moreover, it is important to note that this study focused solely on a truncated segment of the pulmonary bifurcation, with fixed boundary conditions applied at both the inlets and outlets. This modeling constraint inherently limits the vessel's ability to expand freely, potentially underestimating the full extent of physiological deformation that would occur *in vivo*, where the surrounding vasculature provides more compliant support.

IV. DISCUSSION

In this study, the specific pulmonary artery bifurcation was significantly stenosed, and the pre-operative angle was measured at 100°. In clinical practice, the final postoperative geometry, particularly the bifurcation angle, depends on surgical technique, patch configuration, and vessel elasticity. Due to anatomical constraints or the need to reduce tension, surgeons do not always restore the native or typical bifurcation angle.[34]

Since surgical repair alters vessel geometry, we explored the hemodynamic impact of varying this angle to provide biomechanical insights that may inform future surgical optimization. Hence, five bifurcation models were developed by virtually modifying a subject-specific geometry, with angles ranging from 70° to 105°, to replicate potential anatomical variations arising from surgical reconstruction.

The development of arteriosclerotic plaques and neointimal hyperplasia is a complex, multifactorial process, with vascular wall shear stress (WSS) recognized as a key predictive factor.[35–37] The drag force exerted by blood flow on the endothelial surface is transduced into biochemical signals that influence vascular function and structure.

Sustained laminar flow, associated with uniform WSS, is crucial for maintaining endothelial homeostasis and is widely considered a protective factor against atherosclerosis. In contrast, disturbed flow patterns, commonly occurring at arterial bifurcations, branch points, and regions of curvature, are linked to endothelial dysfunction, atheroma formation, and neointimal hyperplasia.

In this context, the results demonstrated that bifurcation angle significantly affects local wall shear stress (WSS), static pressure distribution, and arterial volume changes throughout the cardiac cycle. Among all configurations, the model with $\alpha = 90^\circ$ exhibited the lowest peak WSS and the most uniform time-averaged WSS distribution, suggesting a more favorable shear environment for endothelial health. Additionally, this model showed moderate arterial volume expansion ($\sim$2.6%), indicating a balanced compliance response under pulsatile flow conditions.

In contrast, more acute or obtuse angles ($\alpha = 70^\circ$, 80°, 100°, and 105°) demonstrated elevated WSS levels and greater variability in pressure and volume deformation. Such conditions are known to increase the mechanical load on the vessel wall and may predispose to maladaptive vascular remodeling or localized tissue stress. Based on the combined assessment of WSS uniformity and volume deformation, the $\alpha = 90^\circ$ configuration appears to provide the most balanced biomechanical performance and may represent a more optimal postoperative geometry from a haemodynamic standpoint.

It is important to note that this study was based on a single subject-specific pulmonary artery geometry with a pre-operative bifurcation angle of 100°. While the findings highlight 90° as a potentially favorable configuration for this particular case, the results may not be directly generalizable to the broader population, especially across different age groups or anatomical variations. Vascular geometry, compliance, and flow conditions can vary significantly between individuals due to developmental, pathological, or surgical factors. Therefore, while the trends observed provide valuable insight into angle-dependent haemodynamic behavior, further studies incorporating a larger cohort and broader anatomical variability are needed to confirm the applicability of these findings to better assist clinical decision-making.

In addition, several methodological limitations should also be acknowledged. The numerical model was validated using a carotid artery benchmark rather than a pulmonary artery phantom; experimental validation specific to the pulmonary artery geometry is planned for future work. Although the geometry used was subject-specific, the analysis was limited to variations in the MPA–RPA bifurcation angle, while other anatomical features such as vessel curvature, asymmetry, or wall thickness remained fixed. Additionally, boundary conditions were constrained by fixed inlet and outlet settings, potentially restricting physiologic vessel motion and deformation. The deformation analysis focused solely on internal volume change, without evaluating other mechanical responses, such as wall displacement or bending, which may also influence postoperative performance. While the 90° configuration demonstrated favorable biomechanical indicators in this case, it is not yet clinically validated and may be challenging to reproduce consistently in surgical practice due to anatomical and procedural constraints. Finally, the model was confined to a truncated segment of the pulmonary bifurcation, without accounting for upstream or downstream vascular interactions that could influence the local flow and the vessel behavior.

Nonetheless, this research approach provides a practical and flexible framework for evaluating post-surgical haemodynamics using patient-derived models. It offers a valuable tool for future investigations into more complex or realistic geometries, potentially supporting evidence-based surgical planning and personalized vascular reconstruction.

V. CONCLUSION

This study investigated the influence of bifurcation angle variation at the postoperative junction between the MPA and the RPA on haemodynamic behavior and the arterial wall deformation using fluid–structure interaction simulations. A series of virtual reconstructions were generated by digitally modifying a subject-specific geometry to represent potential outcomes of surgical intervention. The analysis revealed that bifurcation angle plays a critical role in determining local wall shear stress, pressure distribution, and vessel compliance. Among all tested configurations, the model with $\alpha = 90^\circ$ demonstrated a balanced haemodynamic profile, showing the lowest peak wall shear stress ($\sim$45 Pa) and the lowest time-averaged WSS ($\sim$18 Pa) compared with the highest peak value ($\sim$134 Pa) observed at $\alpha = 80^\circ$. Furthermore, the static wall pressure at the bifurcation apex was reduced by approximately 1000 Pa in the FSI model compared with the rigid-wall case, highlighting the damping effect of wall compliance. The arterial volume expansion of 2.6%–2.8% relative to the original lumen volume at $\alpha = 90^\circ$ indicates a moderate and physiologically realistic compliance response under pulsatile flow conditions. Collectively, these results suggest that the 90° configuration provides the most favorable haemodynamic performance, characterized by low and uniformly distributed wall shear stress, moderate arterial deformation, and stable pressure distribution. These findings underscore the importance of considering bifurcation geometry in vascular reconstruction and highlight the value of patient-specific modeling in evaluating postoperative geometries and optimizing vascular reconstruction strategies. Future multi-patient studies are required to establish the broader applicability of these findings and evaluate their potential to provide clinical guidance for real-world implementation.

ACKNOWLEDGMENTS

This work was partially supported by the Australian Research Council (Grant No. DE210101549).

AUTHOR DECLARATIONS

Conflict of Interest

The authors have no conflicts to disclose.

Ethics Approval

Ethics approval has been obtained from the Medical Ethics Committee of Cardiovascular Surgery and the Institutional Review Board of the General Hospital of Northern Theater Command, Shenyang, China (Batch No.: 2020-15). Written informed consent was obtained from the guardians of all pediatric participants prior to their participation in the study.

Author Contributions

Bo Xu: Conceptualization (equal); Data curation (equal); Formal analysis (equal); Investigation (equal); Methodology (equal); Validation

(equal); Visualization (equal); Writing – original draft (equal). **Shaokoon Cheng:** Conceptualization (equal); Methodology (equal); Validation (equal); Writing – review & editing (equal). **Ruiping Ma:** Visualization (equal); Writing – review & editing (equal). **Xiaodong Wang:** Conceptualization (equal); Resources (equal); Supervision (equal). **Yong Zhang:** Resources (equal). **Zhonghua Sun:** Investigation (equal); Writing – review & editing (equal). **Bernard Allard:** Conceptualization (equal); Writing – review & editing (equal). **Jingliang Dong:** Conceptualization (equal); Formal analysis (equal); Funding acquisition (equal); Methodology (equal); Project administration (equal); Resources (equal); Supervision (equal); Validation (equal); Writing – review & editing (equal).

DATA AVAILABILITY

The data that support the findings of this study are available from the corresponding author upon reasonable request.

REFERENCES

[1]World Health Organization, *Birth Defects* (World Health Organization, 2023).
[2]D. van der Linde, E. E. Konings, M. A. Slager, M. Witsenburg, W. A. Helbing, J. J. Takkenberg, and J. W. Roos-Hesselink, "Birth prevalence of congenital heart disease worldwide: A systematic review and meta-analysis," J. Am. Coll. Cardiol. **58**, 2241 (2011).
[3]X. Wang, W. Bakhuis, K. M. Veen, A. J. Bogers, J. R. Etnel, C. C. van Der Ven, J. W. Roos-Hesselink, E.-R. Andrinopoulou, and J. J. Takkenberg, "Outcomes after right ventricular outflow tract reconstruction with valve substitutes: A systematic review and meta-analysis," Front. Cardiovasc. Med. **9**, 897946 (2022).
[4]S. S. Hu, L. Z. Kong, R. L. Gao, M. L. Zhu, W. Wang, Y. J. Wang, Z. S. Wu, W. W. Chen, and M. B. Liu, "Outline of the report on cardiovascular disease in China, 2010," Biomed. Environ. Sci. **25**, 251 (2012).
[5]K. A. Holst, S. M. Said, T. J. Nelson, B. C. Cannon, and J. A. Dearani, "Current interventional and surgical management of congenital heart disease," Circ. Res. **120**, 1027 (2017).
[6]A. F. Corno and E. S. Mickaily-Huber, "Comparative computational fluid dynamic study of two distal Contegra conduit anastomoses," Interact. Cardiovasc. Thorac. Surg. **7**, 1 (2008).
[7]O. Schiller, P. Sinha, D. Zurakowski, and R. A. Jonas, "Reconstruction of right ventricular outflow tract in neonates and infants using valved cryopreserved femoral vein homografts," J. Thorac. Cardiovasc. Surg. **147**, 874 (2014).
[8]S. O. Shebani, S. McGuirk, M. Baghai, J. Stickley, J. V. De Giovanni, F. A. Bu'Lock, D. J. Barron, and W. J. Brawn, "Right ventricular outflow tract reconstruction using Contegra® valved conduit: Natural history and conduit performance under pressure," Eur. J. Cardio-Thorac. Surg. **29**, 397 (2006).
[9]A. L. Marsden, A. J. Bernstein, V. M. Reddy, S. C. Shadden, R. L. Spilker, F. P. Chan, C. A. Taylor, and J. A. Feinstein, "Evaluation of a novel Y-shaped extracardiac Fontan baffle using computational fluid dynamics," J. Thorac. Cardiovasc. Surg. **137**, 394 (2009).
[10]K. R. Kanter, C. M. Haggerty, M. Restrepo, D. A. de Zelicourt, J. Rossignac, W. J. Parks, and A. P. Yoganathan, "Preliminary clinical experience with a bifurcated Y-graft Fontan procedure—A feasibility study," J. Thorac. Cardiovasc. Surg. **144**, 383 (2012).
[11]W. Konertz, E. Angeli, G. Tarusinov, T. Christ, J. Kroll, P. M. Dohmen, O. Krogmann, B. Franzbach, C. Pace Napoleone, and G. Gargiulo, "Right ventricular outflow tract reconstruction with decellularized porcine xenografts in patients with congenital heart disease," J. Heart Valve Dis. **20**(3), 341–347 (2011).
[12]G. Troianowski, C. A. Taylor, J. A. Feinstein, and I. E. Vignon-Clementel, "Three-dimensional simulations in Glenn patients: Clinically based boundary conditions, hemodynamic results and sensitivity to input data," J. Biomech. Eng. **133**, 111006 (2011).
[13]H. Wang, H. Song, Y. Yang, Z. Wu, R. Hu, J. Chen, J. Guo, Y. Wang, D. Jia, S. Cao, Q. Zhou, and R. Guo, "Morphology display and hemodynamic testing using 3D printing may aid in the prediction of LVOT obstruction after mitral valve replacement," Int. J. Cardiol. **331**, 296 (2021).
[14]Y. Bazilevs, M. C. Hsu, Y. Zhang, W. Wang, T. Kvamsdal, S. Hentschel, and J. G. Isaksen, "Computational vascular fluid–structure interaction: Methodology and application to cerebral aneurysms," Biomech. Model. Mechanobiol. **9**, 481 (2010).
[15]F. S. Schoenhoff, O. Loup, B. Gahl, Y. Banz, M. Pavlovic, J.-P. Pfammatter, T. P. Carrel, and A. Kadner, "The Contegra bovine jugular vein graft versus the Shelhigh pulmonic porcine graft for reconstruction of the right ventricular outflow tract: A comparative study," J. Thorac. Cardiovasc. Surg. **141**, 654 (2011).
[16]L. Ma, Y. Liu, X. Zhao, X. Ren, F. Bai, J. Ding, M. Zhang, W. Wang, J. Xie, H. Zhang, Z. Zhao, and H. Han, "Hemodynamic influence of different pulmonary stenosis degree in Glenn procedure: A numerical study," Adv. Mech. Eng. **6**, 472370 (2014).
[17]W. Yang, F. P. Chan, V. M. Reddy, A. L. Marsden, and J. A. Feinstein, "Flow simulations and validation for the first cohort of patients undergoing the Y-graft Fontan procedure," J. Thorac. Cardiovasc. Surg. **149**, 247 (2015).
[18]J. Dong, K. Inthavong, and J. Tu, "Image-based computational hemodynamics evaluation of atherosclerotic carotid bifurcation models," Comput. Biol. Med. **43**, 1353 (2013).
[19]J. Dong, Z. Sun, K. Inthavong, and J. Tu, "Fluid–structure interaction analysis of the left coronary artery with variable angulation," Comput. Methods Biomech. Biomed. Eng. **18**, 1500 (2015).
[20]K. Itatani, S. Miyazaki, T. Furusawa, S. Numata, S. Yamazaki, K. Morimoto, R. Makino, H. Morichi, T. Nishino, and H. Yaku, "New imaging tools in cardiovascular medicine: Computational fluid dynamics and 4D flow MRI," Gen. Thorac. Cardiovasc. Surg. **65**, 611 (2017).
[21]G. Rigatelli, C. Chiastra, G. Pennati, G. Dubini, F. Migliavacca, and M. Zuin, "Applications of computational fluid dynamics to congenital heart diseases: A practical review for cardiovascular professionals," Expert Rev. Cardiovasc. Ther. **19**, 907 (2021).
[22]X. L. Yang, Y. Liu, and J. M. Yang, "Fluid-structure interaction in a pulmonary arterial bifurcation," J. Biomech. **40**, 2694 (2007).
[23]A. D. Bordones, M. Leroux, V. O. Kheyfets, Y.-A. Wu, C.-Y. Chen, and E. A. Finol, "Computational fluid dynamics modeling of the human pulmonary arteries with experimental validation," Ann. Biomed. Eng. **46**, 1309 (2018).
[24]H. Tsubata, N. Nakanishi, K. Itatani, M. Takigami, Y. Matsubara, T. Ogo, T. Fukuda, H. Matsuda, and S. Matoba, "Pulmonary artery blood flow dynamics in chronic thromboembolic pulmonary hypertension," Sci. Rep. **13**, 6490 (2023).
[25]F. Fontan and E. Baudet, "Surgical repair of tricuspid atresia," Thorax **26**, 240 (1971).
[26]J.-B. Moretti, R. Michael, S. Gervais, É. Alchourron, N. Stein, Z. Farhat, C. Lapierre, J. Dubois, and R. El-Jalbout, "Normal pediatric values of carotid artery intima-media thickness measured by B-mode ultrasound and radiofrequency echo tracking respecting the consensus: A systematic review," Eur. Radiol. **34**, 654 (2023).
[27]A. J. Bank and D. R. Kaiser, *Arterial Wall Mechanics* (Springer Berlin Heidelberg, Berlin, Heidelberg, 2002).
[28]C. P. Cheng, R. J. Herfkens, A. L. Lightner, C. A. Taylor, and J. A. Feinstein, "Blood flow conditions in the proximal pulmonary arteries and vena cavae: Healthy children during upright cycling exercise," Am. J. Physiol. Heart Circ. Physiol. **287**, H921 (2004).
[29]F. J. H. Gijsen, F. N. van de Vosse, and J. D. Janssen, "The influence of the non-Newtonian properties of blood on the flow in large arteries: Steady flow in a carotid bifurcation model," J. Biomech. **32**, 601 (1999).
[30]Z. Ding, K. Wang, J. Li, and X. Cong, "Flow field and oscillatory shear stress in a tuning-fork-shaped model of the average human carotid bifurcation," J. Biomech. **34**, 1555 (2001).
[31]N. A. Buchmann, M. Yamamoto, M. Jermy, and T. David, "Particle image velocimetry (PIV) and computational fluid dynamics (CFD) modelling of carotid artery haemodynamics under steady flow: A validation study," J. Biomech. Sci. Eng. **5**, 421 (2010).
[32]N. A. Buchmann, *Development of Particle Image Velocimetry for In-Vitro Studies of Arterial Haemodynamics* (University of Canterbury, Christchurch, 2010).
[33]H. Cheng, W. Zhong, L. Wang, Q. Zhang, X. Ma, Y. Wang, S. Wang, C. He, Q. Wei, and C. Fu, "Effects of shear stress on vascular endothelial functions in atherosclerosis and potential therapeutic approaches," Biomed. Pharmacother. **158**, 114198 (2023).

[34]W. C. Zheng, E. Buratto, F. Caldaroni, S. Ishigami, I. E. Konstantinov, and Y. d'Udekem, "T-remodeling of the pulmonary artery bifurcation for pulmonary artery origin stenosis," World J. Pediatr. Congenital Heart Surg. **14**, 716 (2023).
[35]O. Traub and B. C. Berk, "Laminar shear stress: Mechanisms by which endothelial cells transduce an atheroprotective force," Arterioscler. Thromb. Vasc. Biol. **18**, 677 (1998).
[36]K. S. Cunningham and A. I. Gotlieb, "The role of shear stress in the pathogenesis of atherosclerosis," Lab. Invest. **85**, 9 (2005).
[37]Y. S. Chatzizisis, A. U. Coskun, M. Jonas, E. R. Edelman, P. H. Stone, and C. L. Feldman, "Risk stratification of individual coronary lesions using local endothelial shear stress: A new paradigm for managing coronary artery disease," Curr. Opin. Cardiol. **22**, 552 (2007).